








Article

A Study of the Corrosion Behavior of AHSS Complex-Phase CP 780 Employing an Electrochemical Noise Technique Analyzed by Different Methods

Maria Lara-Banda ¹, Facundo Almeraya-Calderón ¹, Jesús Manuel Jáquez-Muñoz ²,
Demetrio Nieves-Mendoza ³, Miguel Angel Baltazar-Zamora ^{3,*}, Javier Olguín-Coca ⁴,
Francisco Estupiñan-Lopez ¹, Jose Cabral Miramontes ¹, Griselda Santiago-Hurtado ⁵
and Citlalli Gaona-Tiburcio ^{1,*}

- ¹ Centro de Investigación e Innovación en Ingeniería Aeronáutica (CIIA), s/n, Faculty of Mechanical and Electrical Engineering, Universidad Autónoma de Nuevo León, Ciudad Universitaria, San Nicolás de los Garza 66455, Mexico; maria.laraba@uanl.edu.mx (M.L.-B.); facundo.almerayacl@uanl.edu.mx (F.A.-C.); francisco.estupinanlp@uanl.edu.mx (F.E.-L.); jose.cabralmr@uanl.edu.mx (J.C.M.)
- ² Instituto Tecnológico de Ciudad Juárez, Av. Tecnológico, 1340, Ciudad Juárez 32500, Mexico; jesus.jaquezmn@uanl.edu.mx
- ³ Facultad de Ingeniería Civil, Universidad Veracruzana, Xalapa 91000, Mexico; dnieves@uv.mx
- ⁴ Área Académica de Ingeniería y Arquitectura, Universidad Autónoma del Estado de Hidalgo, Carretera Pachuca-Tulancingo Km. 4.5., Pachuca 42082, Mexico; olguinc@uaeh.edu.mx
- ⁵ Facultad de Ingeniería Civil, Universidad Autónoma de Coahuila, Torreón 27276, Mexico; santiagog@uadec.edu.mx
- * Correspondence: mbaltazar@uv.mx (M.A.B.-Z.); citlalli.gaonatbr@uanl.edu.mx (C.G.-T.)



Academic Editors: Fei Yin, Jian Wang and Lin Hua

Received: 15 November 2024

Revised: 27 December 2024

Accepted: 3 January 2025

Published: 11 January 2025

Citation: Lara-Banda, M.; Almeraya-Calderón, F.; Jáquez-Muñoz, J.M.; Nieves-Mendoza, D.; Baltazar-Zamora, M.A.; Olguín-Coca, J.; Estupiñan-Lopez, F.; Cabral Miramontes, J.; Santiago-Hurtado, G.; Gaona-Tiburcio, C. A Study of the Corrosion Behavior of AHSS Complex-Phase CP 780 Employing an Electrochemical Noise Technique Analyzed by Different Methods. *Metals* **2025**, *15*, 59. <https://doi.org/10.3390/met15010059>

Copyright: © 2025 by the authors. Licensee MDPI, Basel, Switzerland. This article is an open access article distributed under the terms and conditions of the Creative Commons Attribution (CC BY) license (<https://creativecommons.org/licenses/by/4.0/>).

Abstract: The automotive industry employs structural steels with E-coats to reduce weight and increase the corrosion resistance of chassis, reducing CO₂ emissions. Due to their mechanical properties, part of the chassis is a composite of advanced high-strength steels (AHSS). AHSSs are coated by conversion methods such as phosphate to increase epoxy coating adherence and corrosion resistance. The main point of this research is to characterize an AHSS complex-phase (CP) 780 in blank, with a phosphate coating and an E-coat organic coating using electrochemical noise, employing time-domain, frequency-domain, time-frequency-domain, and chaotic system methods to determine the type and corrosion kinetics of each system. The electrochemical noise technique was made with a conventional three-electrode cell, using a saturated calomel as a reference electrode. Data were recorded at 1024 s, at 1 data per second in a 3.5 wt. % NaCl electrolyte, according to ASTM G199-09. The results show how AHSS CP 780 presented uniform corrosion, similarly to the phosphate sample; however, the E-coat presented a trend of a localized process when analyzed by Wavelets transform. On the other hand, corrosion resistance increased for the E-coat sample, with values of $2.58 \times 10^6 \Omega \cdot \text{cm}^2$. According to the results of the research, all the samples are susceptible to present localized corrosion.

Keywords: E-coat; electrochemical noise; chaos theory; corrosion; AHSSs

1. Introduction

The automotive industry has been looking for ways to increase the efficiency of vehicles to reduce CO₂ emissions and gas consumption; however, those aspects have financial and environmental impacts, so it is important to consider the selection of materials [1,2]. The vehicle chassis is made of advanced high-strength steels (AHSSs) with a high-property

specter in the function of the microstructure and grade. Steels such as CP (complex phase), that present excellent mechanical properties, integrate the AHSSs [1–5]. Nowadays, the steel CP780 is employed in chassis impact zones due to the high energy absorption inside of the chassis, in panel interiors, and in the components of security cages [6,7]. CP steels are a mixed microstructure with a ferrite/bainite matrix containing fractions of retained austenite, martensite, and pearlite (ferrite + iron carbide). The grain must be refined in these steels to obtain the desired properties; delayed recrystallization is often employed to develop very small grains for a very fine microstructure. Microalloying elements such as niobium or titanium may also be precipitated. Complex-phase steel has a fine microstructure that gives high YS and elongation at tensile strengths, similar to dual-phase steels. Additionally, CP steels have good wear characteristics and fatigue strength and can be hardened by heat treatment [8–10].

According to NACE, in 2013, corrosion generated 2.5 trillion dollars in losses [11–13]. Several corrosion processes occur, namely generating an oxide layer due to environmental conditions, exposure to the marine environment, de-icing salts, and surface treatments employed in winter. All these factors decrease safety and, consequently, the useful life of the material, engendering the necessity of employing different techniques to protect the materials [12,14,15].

Much research has been conducted on different conversion coatings (chromate, phosphate, etc.) used to increase the adherence of an epoxy coating to the substrate and the corrosion resistance [16–18]. The phosphate coating, particularly zinc phosphate (tricationic), is one of the most employed pretreatments used by the automotive industry due to its porous structure, because the coating's corrosion mechanisms, involved in all aspects from the corrosive species through to the transportation, are substantial in determining the lifetime of the coating [16,19–22].

In recent years, the automotive industry has been trying to compare the corrosion and the grade of degradation that occurs on car components by employing electrochemical techniques. This happens because the results obtained in electrochemical tests directly correlate with the real environmental corrosion [23–28].

CP780 can present corrosion problems, such as hydrogen-induced corrosion or galvanic corrosion. They showed more susceptibility to corrosion when exposed to NaCl. The corrosion in that medium is a galvanic, wherein hydrogen has an important role [29]. Some added coatings (such as Zn) induce galvanic corrosion; for that reason, it is important to select the correct coating [30]. Zn coatings are the most employed for AHSSs used in the automotive industry; however, those coatings generate a galvanic corrosion process in the material and make the material susceptible to localized corrosion [31,32].

Valenzuela et al. [33] mentioned the susceptibility of AHSSs to environmental hydrogen embrittlement. This occurs due to hydrogen generation, systems where iron water exists, or the porous structure causing hydrogen reactions. The hydrogen reactions occur due to cathodic reactions. Equation (1) shows the reaction that generates the hydrogen [34]:



AHSS presents corrosion problems, which are reduced in phases with retained austenite; when austenite increases, the corrosion rate decreases [35–37]. Also, Franceschi et al. [38] mentioned that when the amount of bainite increases, the corrosion rate increases because the amount of the bainite phase trends to corrosion. In some steels, it is common that a passivation layer helps to reduce the corrosion process; however, in AHSS, it has been registered that in aggressive environments such as NaCl, the material presented active behavior, indicating that passivation did not occur [38,39]. Jabłońska et al. [40] mentioned

that steels present low pitting resistance in NaCl at 3.5 wt. %, so the AHSSs are susceptible to present localized corrosion processes.

It has been reported that the corrosion rate of micro-alloyed steels depends on microstructures. Two phases allow micro-galvanic corrosion cells to generate the corrosion process in preference phases [41,42]. The formation of martensite increases the corrosion resistance of CP steels. However, when martensite is localized with ferrite, the ferrite acts as an anode, and a dissolution process occurs [43–45]. On the other hand, when bainite is in the microstructure with ferrite, the bainite acts as an anode, being dissolved [8].

Electrochemical noise refers to the spontaneous low-level potential and current variations that occur during an electrochemical process. Although the EN specializes in localized processes, it may be used to monitor various corrosion processes; the type of analysis is correlated with the signal type in the system. The effectiveness of EN as a non-perturbative method in localized processes is one of its benefits [46–50].

Time-domain, frequency-domain, frequency–time, and chaotic systems are the different categories into which EN analysis falls. In the early years of the technique, the signal was analyzed using a statistical analysis. Among others, Mansfeld, Cottis, Turgosse, Eden, and Bertocci worked to relate the type of corrosion with statistical parameters like the pitting index (based on the standard deviation of ECN and EPN) and localization index (LI). Additionally, a kinetic variable was related to the noise resistance (R_n) parameter, which was obtained and used as a homolog of R_p . Additionally, some writers [51–57] improved the LI to identify the kind of corrosion by using kurtosis and skewness.

A standard deviation from time-series values (EPN and ECN) must be obtained to calculate noise resistance (R_n). The statistical values in Equation (2) provide details on the causes and dynamics of corrosion. Turgoose and Cottis [57] discovered a correlation between rising corrosion rate and rising variance and standard deviation.

$$R_n = \frac{\sigma_v}{\sigma_I} * A \quad (2)$$

In this investigation, kurtosis and skewness were employed to determine the type of corrosion. Because Mansfeld and Sun [58] determined in 1995 that the localization index (L.I.) had limitations and should be utilized cautiously, it was not considered. A 2001 patent by Reid and Eden [55] states that the third and fourth statistical moments, respectively, skewness and kurtosis (Equations (3) and (4)), can be used to determine the kind of corrosion [59,60]:

$$\text{skewness} = \frac{1}{N} \sum_{i=1}^N \frac{(x_i - \bar{x})^3}{\sigma^3} \quad (3)$$

$$\text{kurtosis} = \frac{1}{N} \sum_{i=1}^N \frac{(x_i - \bar{x})^4}{\sigma^4} \quad (4)$$

For PSD analysis, it is necessary to transform the time-domain EN to the frequency domain by applying a fast Fourier transform (FFT). Since there is a correlation with the EN signal (with a polynomial filter applied), the spectral density is calculated with Equations (5) and (6) [61–63].

$$R_{xx}(m) = \frac{1}{N} \sum_{n=0}^{N-m-1} x(n) \cdot x(n+m), \text{ when values are from } 0 < m < N \quad (5)$$

$$\Psi_x(k) = \frac{\gamma \cdot t_m}{N} \cdot \sum_{n=1}^N (x_n - \bar{x}_n) \cdot e^{-\frac{2\pi i k n^2}{N}} \quad (6)$$

To advance the study, several writers divided the signal on the crystal, often from 1 to 8, and created an energy map by decomposing the signal using the Wavelets transform.

The authors connected metastable pitting to the first crystal energy, D1 to D3. Localized corrosion is linked to crystals D4 through D6, whereas diffusion and regulated processes (uniform corrosion) are linked to crystals D7 and D8. The EN signal's DC signal is linked to the S8 crystal [64–68]. Wavelets use a high–low filter to break down a signal; low frequencies are called approximations, and high frequencies are called details [67]. The total energy of an N number of data points is given in Equations (7)–(9).

$$E = \sum_{n=1}^N x_n^2 \quad (7)$$

Additionally, Equation (11) provides energy fractions of details and approximation:

$$ED_j^d = \frac{1}{E} \sum_{n=1}^N d_{j,n}^2 \quad ED_j^s = \frac{1}{E} \sum_{n=1}^N s_{j,n}^2 \quad (8)$$

Equation (12) states that the total energy evaluated is equal to the energy of each wavelet transform component:

$$E = ED_j^s \sum_{j=1}^j ED_j^d \quad (9)$$

Recurrence plots are a valuable tool for nonlinear system analysis. Various methodologies must be used to assess the type and progress of corrosion on the surface because corrosion is a chaotic and nonlinear system. A practical method for obtaining that analysis is RP.

Recurrence plots are time-function-realized, two-dimensional graphs. The path of x_i in R_m , where m is the spatial dimension, is given to i and j at a time interval of ε . The times t_i and t_j from two dimensions are displayed as a two-dimensional square matrix by the RP. The matrix is displayed in Equation (4) [68–74]:

$$R_{ij}(\varepsilon) = \Theta\left(\varepsilon - \|\vec{x}_i - \vec{x}_j\|\right), i, j = 1, \dots, N \quad (10)$$

where $\|\cdot\|$ is the norm (Euclidean, maximum, or Manhattan), μ is the distance umbral, $\Theta(x)$ is the Heaviside function, and N is the number of data or points x_i . Equation (4) illustrates the recurrence rate, which determines the recurrence density:

$$RR(\varepsilon) = \frac{1}{N^2} \sum_{i,j=1}^N R_{i,j} \quad (11)$$

In an umbral zone, the recurrence rate (RR) indicates the likelihood of reconstructing a single track.

The diagonal lines of RP show the system's determinism and how the trajectory has changed over time in the phase space. The determinism (DET) is computed using the following equation:

$$DET = \frac{\sum_{l=l_{\min}}^N lp(l)}{\sum_{l=1}^N lp(l)} \quad (12)$$

Long diagonal lines on the RP are necessary for periodicity, and DET approaches unity; stochastic signals result in solitary dots, which restrict DET to values near zero. The average diagonal line length (L), another RQA metric associated with diagonal lines, is as follows in Equation (13):

$$L = \frac{\sum_{l=l_{\max}}^N lp(l)}{\sum_{l=l_{\min}}^N p(l)} \quad (13)$$

TT gives the vertical structures' average length and the system's average time.

$$TT = \frac{\sum_{v=v_{\min}}^N vP(v)}{\sum_{v=v_{\min}}^N P(v)} \quad (14)$$

The electrochemical phenomenon that takes place throughout the corrosion process is described by the electrochemical noise (EN) technique. The Hilbert–Huang analysis is one methodology used to describe the EN method. This technique facilitates the frequency and timing of energy exchanges; the energy, known as instantaneous energy, is derived from the signal's inherent function and is retrieved by signal decomposition [72,75]. Equation (9) explains the empirical method of decomposition (EMD):

$$x(t) = \sum_{i=1}^N h^{(i)}(t) + d(t) \quad (15)$$

where $d(t)$ is the average of the trend at a low frequency of the time series $x(t)$ and cannot be decomposed; $h^{(i)}(t)$ is the i -th term of IMF that is generated; these numbers must satisfy the conditions that the extreme and cross numbers are equal or differ by a maximum of 1 and that each point using the local maximum and minimum must be 0. The HHT is represented by Equation (10):

$$y_j(t) = \frac{1}{\pi} p \int_{-\infty}^{\infty} \frac{h_j(\tau)}{t - \tau} d\tau \quad (16)$$

where p is connected to the Cauchy principle and is associated with an average of IMF; $y_j(t)$ is the Hilbert transform; and IMF is represented by h_j .

This work aimed to evaluate the electrochemical corrosion behavior of AHSS CP780 without treatment, broken down into components called the substrate, the phosphate, and the CP780 with the E-coat. The electrochemical noise technique was employed to study samples using time-domain (statistical), frequency-domain (PSD), time–frequency-domain (Wavelets and Hilbert–Huang) methods, and recurrence plots for chaotic analysis. The electrolyte used is NaCl at 3.5 wt. %, simulating a marine environment.

2. Materials and Methods

2.1. Materials

Complex-phase (CP) steel is a predominant AHSS steel grade currently in commercial use, designated as CP780 ($R_m = 780$ MPa). Its microstructure contains small amounts of martensite, retained austenite, and pearlite within a ferrite/bainite matrix. An AHSS CP780 laminate of 10×30 cm was employed. The chemical composition was determined by atomic absorption spectroscopy (AAS) (see Table 1).

Table 1. Chemical composition of AHSS CP780.

AHSS CP780										
Element (wt. %)	C	Mn	Ti	P	Cr	S	Si	Nb	Al	Fe
	0.091	1.669	0.007	0.010	0.771	0.002	0.511	0.045	0.034	Balance

2.2. Microstructural Characterization

The samples of the AHSSs were prepared by the metallography technique [75], using different SiC grit papers with grades up to 4000. A 0.1 μm aluminum suspension was subsequently used. The chemical etching of the samples was carried out using 5 wt. % Nital solution. Finally, the microstructure of specimens was examined by scanning electron microscopy (SEM, JEOL-JSM-5610LV, Tokyo, Japan) using a secondary electron (SE) detector at a magnification of $2000\times$. AHSS samples were ground to 800-grit SiC paper for electrochemical corrosion testing.

2.3. Electrochemical Characterization

A standard three-electrode cell was utilized for the electrochemical experiments conducted at room temperature. A saturated calomel electrode served as the reference, and the

working (CP780) and auxiliary electrodes were identical. Following ASTM G199-09, EN measurements were performed [75–77]. A scanning speed of 1 data/s was used to measure 2048 data in each trial. The current and potential time series were visually inspected to characterize the behavior of the frequency and amplitude of fluctuations as a function of time and to interpret the signal transients. The electrolytes utilized were solutions of NaCl at 3.5 wt. %. Duplicate tests were conducted. ACM Instruments' Gill-AC potentiostat/galvanostat/ZRA (Zero Resistance Ammeter) was used to record the electrochemical noise measurements concurrently (Manchester, UK). Tests were realized in triplicate [77,78].

A program created in MATAB 2020a software (Math Works, Natick, MA, USA) was used to process the data. Statistical information (R_n , kurtosis, and skewness) was extracted from the signal without DC in the time-domain analysis after the DC trend signal was eliminated from the original EN signal using the polynomial approach. PSD (power spectral density) data were subjected to a Hann window before being converted to the frequency domain using a fast Fourier transform (FFT) for frequency-domain analysis. In order to extract the DC from the EN signal, the orthogonal wavelet transform was applied to the original signal (with DC) in frequency–time-domain analysis energy dispersion graphs (EDP). In order to obtain the intrinsic functions (IMF) of the EN signal using an empirical decomposition method (EMD), EN analysis with the Hilbert–Huang transform (HHT) was required. Lastly, a Hilbert spectrum was used to visualize the instantaneous frequencies.

3. Results

3.1. Microstructure

Figure 1a shows the microstructure of CP780 observed by SEM, where the martensite structure (M), retained austenite (RA), and ferrite (F)/bainite (B) matrix can be observed. Figure 1b shows the CP780 steel phases at a higher magnification of 5000 \times , and Figure 1c shows the composition of the EDS specter with the alloying elements.

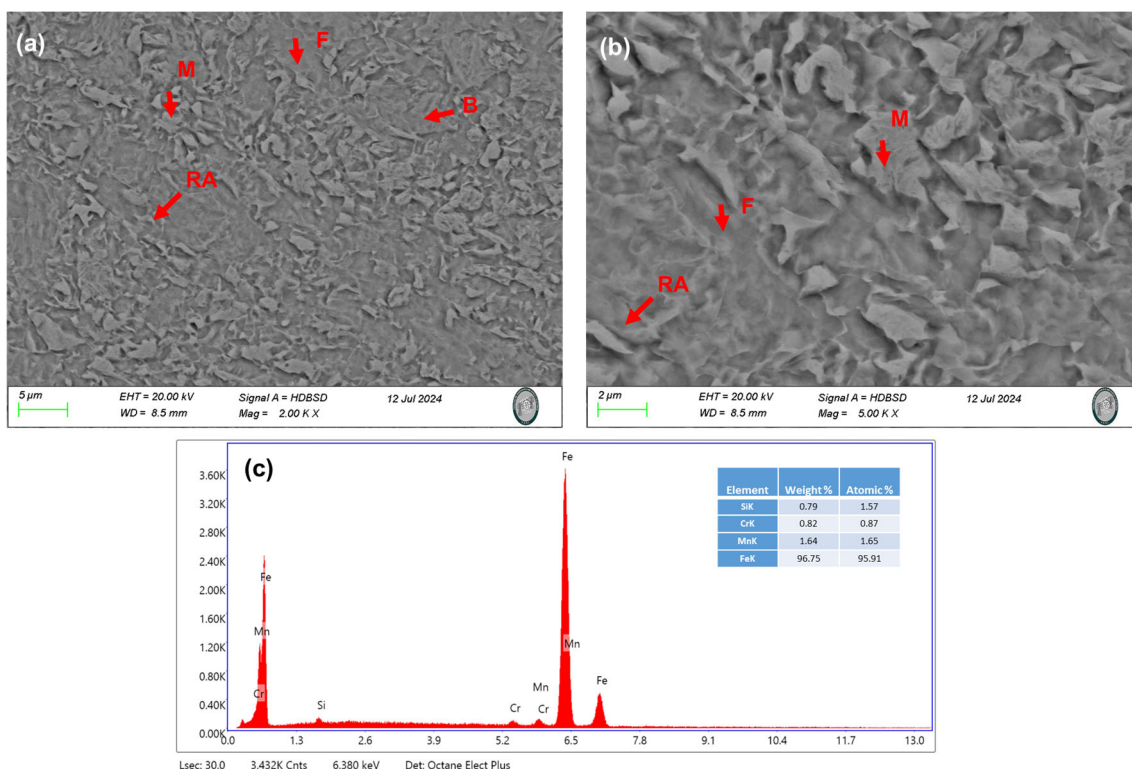


Figure 1. SEM Superficial morphology of AHSS CP780: (a) microstructure, 2000 \times ; (b) microstructure, 5000 \times ; and (c) EDS specter.

3.2. Electrochemical Noise

3.2.1. Time-Domain Analysis

The use of the electrochemical noise technique for the investigation and monitoring of corrosion has allowed for many advances in recent years that are interesting for corrosion science. A particular advantage of electrochemical noise measurements is the possibility to detect and analyze the localized corrosion. Electrochemical noise describes the spontaneous low-level potential and current fluctuations that occur during an electrochemical process. These transients manifest in potential and current noise that can be exploited in a corrosion map [76–78]. Transients are linked to anodic and cathodic reactions as a result of stochastic processes (the rupture and re-passivation of the passive film) and deterministic processes (the formation and propagation of pitting).

Figure 2 shows the EN signal processed in the time domain when exposed to NaCl at 3.5 wt. %. Figure 2a shows that the EPN substrate presented a signal with a high amplitude of values of 3×10^{-3} V. The signals of the phosphate and substrate presented transients of high frequency. Figure 2b shows the ECN signal; in that figure, the substrate signal presents high amplitude oscillations (3×10^{-6} A/cm²); usually, that behavior is associated with high corrosion kinetics. On the other hand, the E-coat presented low amplitude oscillations with values in the $\times 10^{-9}$ A/cm² order. Figure 2c shows a windowing of the E-coat current noise signal, to better observe the fluctuations in time.

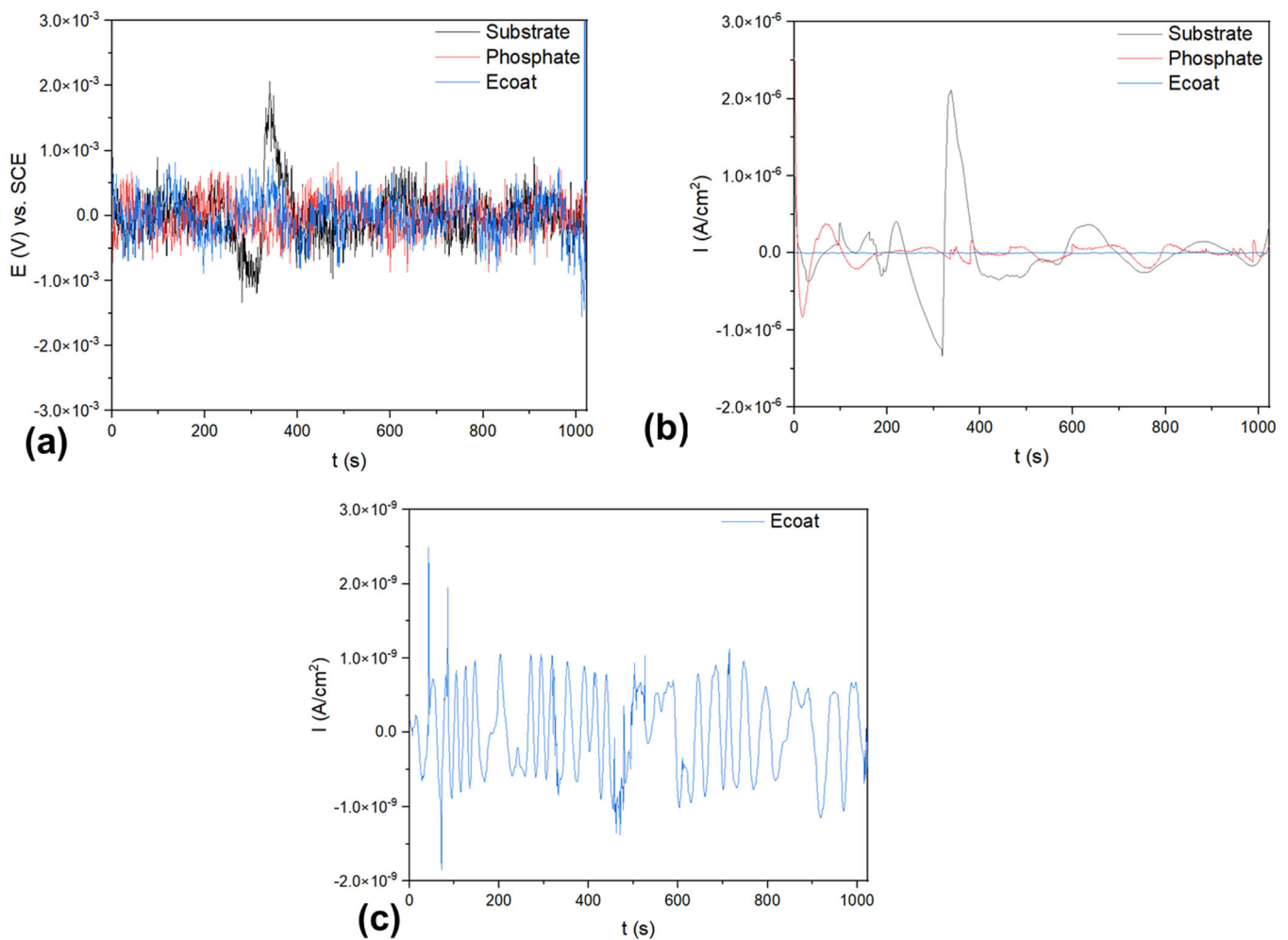


Figure 2. Electrochemical potential (a) and current (b) noise time-series exposed to 3.5 wt. % NaCl solution, and (c) windowing ENC signal of the E-coat.

Table 2 shows the statistical parameters obtained from the ECN signal. The substrate presented lower corrosion resistance, with values of $9.31 \times 10^2 \Omega \cdot \text{cm}^2$; on the other hand, the E-coat presented a value of $94.85 \times 10^4 \Omega \cdot \text{cm}^2$. When determining the corrosion type, statistical analysis generates uncertainty due to the E-coat’s presented values of LI related to localized processes and kurtosis; however, in the skew, the value is associated with uniform corrosion. Something similar occurs with the substrate and phosphate coating, where the results do not match a specific corrosion type.

Table 2. Statistics parameters obtained from time-domain analysis.

Sample	$R_n (\Omega \cdot \text{cm}^2)$	LI	Corrosion Type	Kurtosis	Corrosion Type	Skew	Corrosion Type
Substrate	$9.31 \times 10^2 \pm 40$	0.04 ± 0.005	Mixed	9.7 ± 2	Localized	3 ± 0.5	Localized
Phosphate	$1.5 \times 10^3 \pm 59$	0.008 ± 0.001	Uniform	60 ± 7	Localized	4.7 ± 0.6	Localized
E-coat	$94.85 \times 10^4 \pm 78$	0.9 ± 0.08	Localized	2.3 ± 0.9	Localized	0.0054 ± 0.0002	Uniform

3.2.2. Power Spectral Density and Noise Impedance

Figure 3 shows the PSD in the current and the noise impedance (Z_n) graphics. Figure 3a shows the PSD in the current; the value ψ^0 from Table 3 can be observed in Figure 3a, where the substrate presented -113 dBi , indicating a faster corrosion kinetic. Figure 3b of Z_n corroborates that value, with $784 \Omega \cdot \text{cm}^2$. The CP780 coating with phosphate presented values of -123 dBi and $1979 \Omega \cdot \text{cm}^2$, indicating that the coating alloy’s corrosion resistance increased. For the E-coat sample, corrosion resistance increased significantly, obtaining -170 dBi and $25.82 \times 10^5 \Omega \cdot \text{cm}^2$, suggesting that coating increases the anticorrosive properties of CP780. The PSD behavior at high frequencies shows that the E-coat is more stable, indicating that the corrosion process does not change.

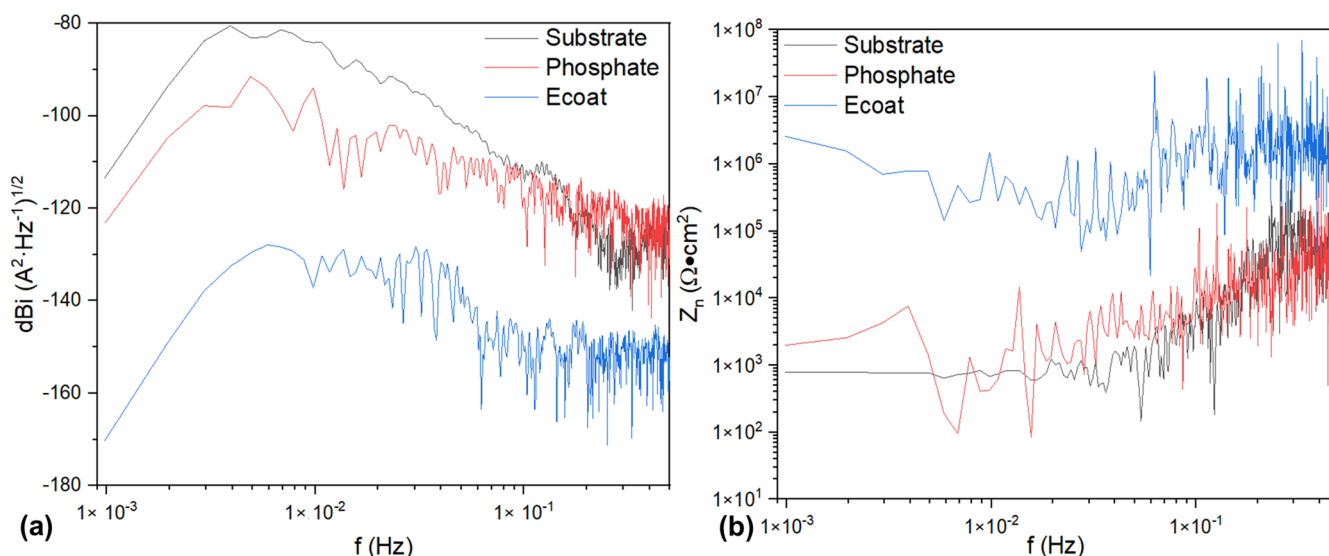


Figure 3. PSD analysis for (a) current signal and (b) noise impedance (Z_n).

Table 3. Parameters obtained from PSD.

Sample	$\psi^0 \text{ (dBi)}$	$Z_{n0} (\Omega \cdot \text{cm}^2)$
Substrate	-113	784
Phosphate	-123	1979
E-coat	-170	25.82×10^5

3.2.3. Wavelets Analysis

The Wavelets analysis from Figure 4 shows how the E-coat presented high energy at the middle crystals; that behavior is related to the localized corrosion process. On the other hand, the substrate and phosphate presented lower energy, and magnification was necessary (Figure 4b), indicating the energy from crystals 5 to 8 accumulated, allowing for a uniform corrosion process to occur. For those samples, the energy begins to accumulate in the middle crystals, indicating that a localized process begins to occur, and after that, it is converted into a uniform process. This can be associated with a uniform pitting corrosion process for substrate and phosphate samples. At the same time, the E-coat only presented a localized process for the energy accumulated in crystals from 3 to 5, with a reduction in energy from 6 to 8. To corroborate these results, it is necessary to complement HHT and the recurrence plots.

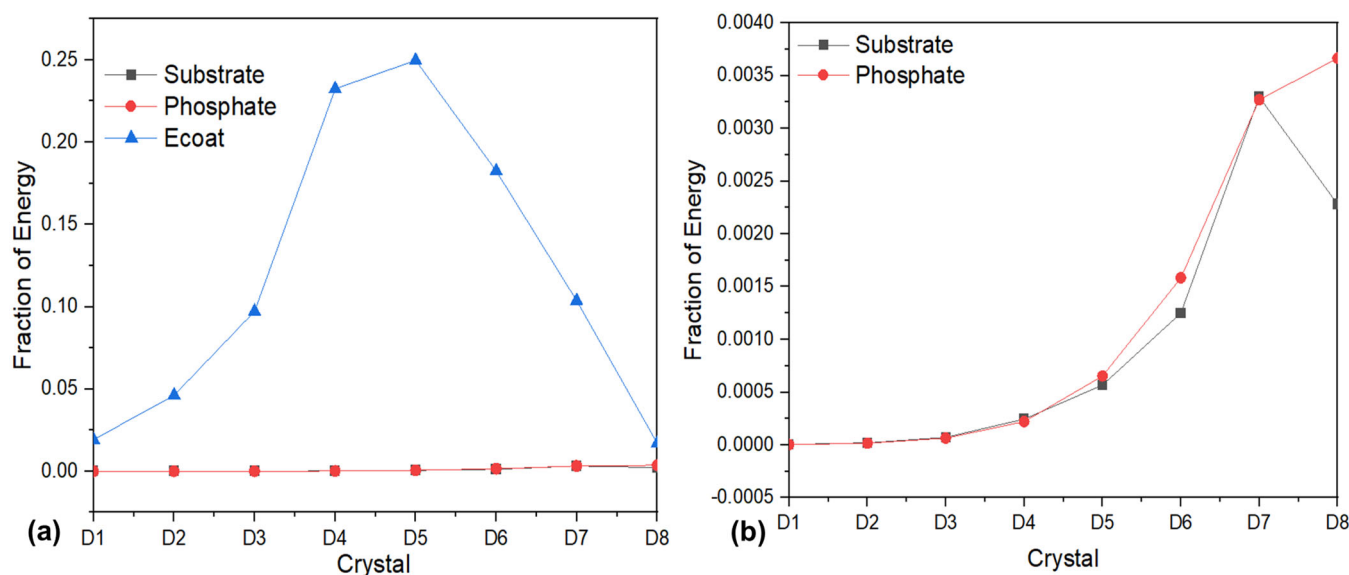


Figure 4. Energy dispersion plots (EDPs) from Wavelets analysis. (a) General analysis and (b) analysis for substrate and phosphate samples.

3.2.4. Hilbert–Huang Transform and Recurrence Plot Analysis

Figure 5 shows the recurrence plot, HHT, and microscopy analysis, allowing for a comparison of the results obtained by those analyses and what occurred on the surface. Figure 5 shows the results obtained for CP780 without coating; an energy accumulation between the second 300 and 400 indicates that a localized process occurred on the surface. However, it is important to mention that the localized process occurred at the second 100, before 200, and a few before 400. After that, energy and events are at low frequencies, indicating that a general corrosion process occurred on the material surface, as shown in the microscopy analysis, where if well pitting is present, the general surface presents a corrosion attack. This can be related to the propagation of localized attacks in preferential zones.

Figure 6 shows similar behavior, where a localized process occurred within the first few seconds, but after some exposition time, the localized attacks began to present uniformly; however, the velocity is lower due to a more localized process occurring. In RP, in the final few seconds, between 900 and 1024 localized processes occurred, which indicates that the diffusion process does not occur as fast as in the uncoated alloy.

On the other hand, Figure 7 shows localized corrosion behavior with the E-coat. This behavior is important because it indicates two things: the first is that the corrosion mechanism changes when the E-coat is applied, and the second is that the coating presents

heterogeneities on a surface; for that reason, the E-coat is not homogenous and has preferred zones for corrosion attacks.

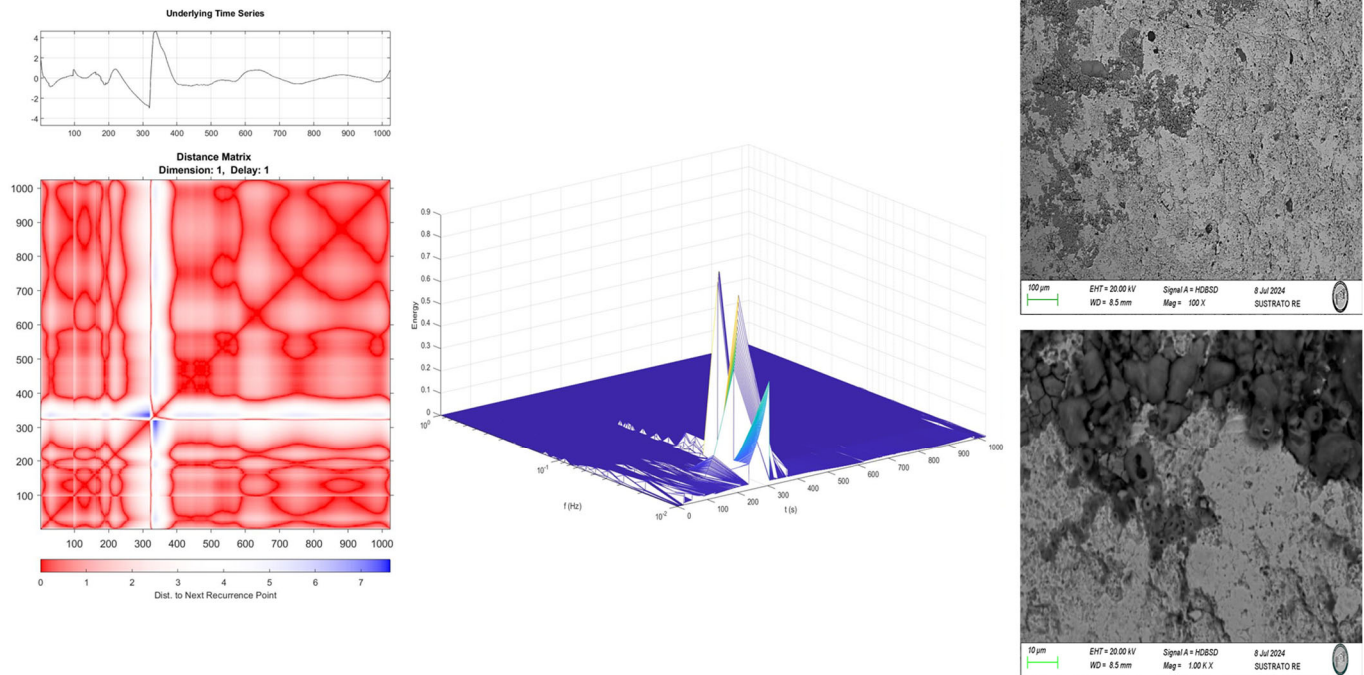


Figure 5. Recurrence plots, Hilbert specter, and microscopy analysis for CP780/substrate.

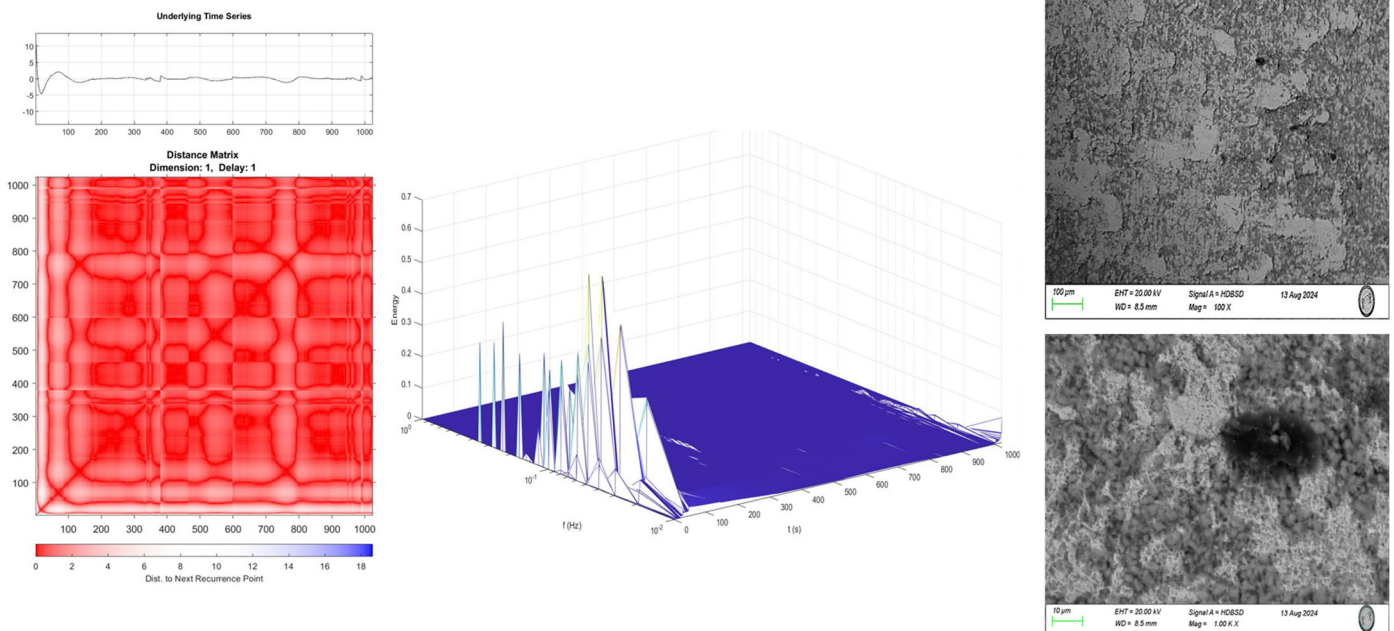


Figure 6. Recurrence plots, Hilbert specter, and microscopy analysis for CP780/phosphate.

The values obtained in Table 4 show how the recurrence is low for the substrate and the E-coat, indicating that a similar process occurs on the surface; however, the deterministic value is lower for E-coat, relating that value with the localized process when the determinism is higher than the value is associated with a uniform corrosion process. That behavior is also shown in laminarity, TT , and T_2 , where the latter is related to the frequency at which some process occurs.

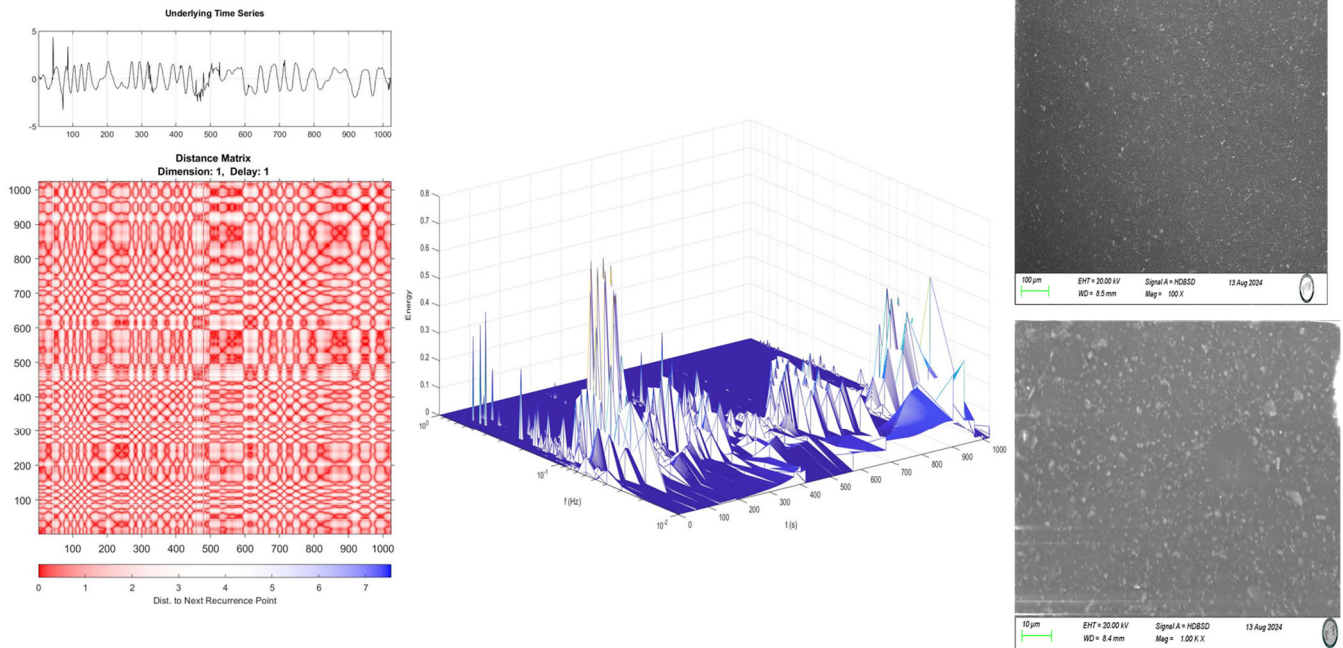


Figure 7. Recurrence plots, Hilbert specter, and microscopy analysis for CP780/E-coat.

Table 4. Parameters obtained by recurrence plot analysis.

Sample	NaCl Solution				
	RR	Det	LAM	TT	T ²
Substrate	0.010 ± 0.002	0.98 ± 0.04	0.99 ± 0.007	10.8 ± 0.01	97.4 ± 0.7
Phosphate	0.12 ± 0.03	0.86 ± 0.007	0.911 ± 0.01	0664 ± 0.6	35.6 ± 0.6
E-coat	0.078 ± 0.002	0.62 ± 0.004	0.75 ± 0.003	3.47 ± 0.004	27.5 ± 0.57

4. Discussion

In the electrochemical noise time-series, the absence of the passive layer is observed, and the metallurgical heterogeneities in the metal matrix determine the corrosion process of this alloy type [79,80]. Localized attacks are facilitated by cathodic and anodic zones brought on by phase differences, grain variations, contaminants, and a lack of homogeneity. Galvanic corrosion is caused by the phase difference in these alloys [81]. In this case, the multiple phases of CP780 facilitate the galvanic couple process, and the presence of elements such as martensite, retained austenite, and ferrite that can act as a cathode, and the presence of bainite that is a natural anode, including the superficial defects, make it prone to localized attacks to the material surface, which, after some exposure time will convert to a general corrosion process due to the galvanic couple.

Two corrosion processes govern the corrosion process of CP780. In those processes, active oxidation is produced by reactions; when oxygen diffuses over the surface, the corrosion products become porous and do not passivate the surface. This makes it easier for Cl⁻ ions to attack the ferrite phase, resulting in a limited attack and preventing the passivation of pitting that forms on the ferrite zone's surface [82]. The subsequent reactions govern the chemical reactions:



Because ferrite and martensite have cathode roles due to oxygen reception, ferrite acts as an anode because of its low O_2 content, which makes it vulnerable to OH^- and Cl^- attacks [83,84]. The presence of Cl^- ions inhibits the generation of a stable oxide layer on the metal surface. This occurs because Cl^- attacks the surface, breaking the passive layer and introducing it as an interstitial ion, provoking an unstable surface and making the material susceptible to localized attacks.

According to the statistical method, the corrosion type does not coincide in nearly all cases. Because of this, you should utilize LI to identify the type of corrosion at your judgment. In order to lower the standard deviation and provide a more precise result, the statistical method's analysis of the signal must also not show a DC signal [85]. Confusion arises when studying the system, because the values obtained by LI in this study do not converge with those obtained by skewness, kurtosis, Wavelets, slope, HHT, and THE RPs in nearly all outcomes. The LI behavior was somewhat certain in steels, but this approach has drawbacks.

While kurtosis established a confined process and skewness presented results of uniform corrosion in different alloys, something similar happened with kurtosis and skewness compared to LI for this study, where the results do not match. This is caused by the limitations of statistics and traditional approaches when studying complicated systems like corrosion. It is also crucial to note that the skewness results in this study showed greater certainty in identifying a corrosion process than kurtosis [36,41,86–88].

The results of R_n , ψ^0 , and Z_n0 reflect congruence; CP780 presented values of 9.31×10^2 , $7.84 \times 10^2 \Omega \cdot \text{cm}^2$, and -113 dBi , respectively, indicating a higher corrosion kinetic, with the pretreatment of phosphating the results presenting 1.5×10^3 , $1.979 \times 10^3 \Omega \cdot \text{cm}^2$, and 123, indicating a reduction in corrosion resistance. However, samples with the E-coat presented values of 94.85×10^4 , $25.82 \times 10^5 \Omega \cdot \text{cm}^2$, and -170 dBi , indicating that the coating increases the corrosion resistance of the material. Diverse authors suggest that R_n and Z_n are homologous in resistance to polarization, so high values of R_n and Z_n are associated with higher corrosion resistance.

The Wavelets analyses are employed to analyze dynamics systems; for this research, the Wavelets analysis showed that only the E-coat presented localized corrosion, due to the energy accumulation at middle crystals that occurs because the coating presents heterogeneities in the surface. The results of RPs and HHT showed high activity at low frequencies, which was favorable for starting some localized attacks, since bainite's dissolution process was formed in a uniform shape. Additionally, some authors believe that the corrosion process in this class of alloys is not limited to the galvanic pair; complex-phase steels can also undergo auto-corrosion [89–92]. In earlier research, Calabrese et al. [89] found that HHT data analysis is a better way to assess EN than Wavelets; this finding was validated in this study, and HHT is superior to statistical analysis in identifying the kind and process of corrosion.

EN's results show how corrosion begins as a localized process and ends as a uniform corrosion process. That result can be observed more with the HHT and RP methods, due to the type of signal. When conventional statistical methods are used to realize an analysis, they present some divergence, which can also occur due to the two corrosion processes in the system. For those cases, it is recommended that a statistical section analysis be carried out. On the other hand, the results obtained from R_n and Z_n are convergent, showing a coherent relationship between the corrosion rates of the two methods.

The authors related the corrosion process of CP and DP steels with the residual stress in martensite formation and the extensive micro-galvanic cell formation between martensite and other phases [6,92–94]. Also, ferrite's high resistance to corrosion compared with bainite influences galvanic cell generation. It occurs due to the bainite having less Cr in

that phase, and the corrosion process occurs more easily. Figure 6 explains the corrosion mechanism; at stage I, a fast diffusion of OH^- begins to attack the surface, and after pitting by OH^- occurs, Cl^- ions attack the surface (stage II), making the corrosion pitting more severe and degrading the material (stage III). As corrosion occurred on the bainite phase, and the bainite phase is dissolute, the rest of surface is eroded from the surface (stage IV); for that reason, a localized attack within the first few seconds of expositions is converted to a localized attack, as is shown in Figure 8 [10,95–97].

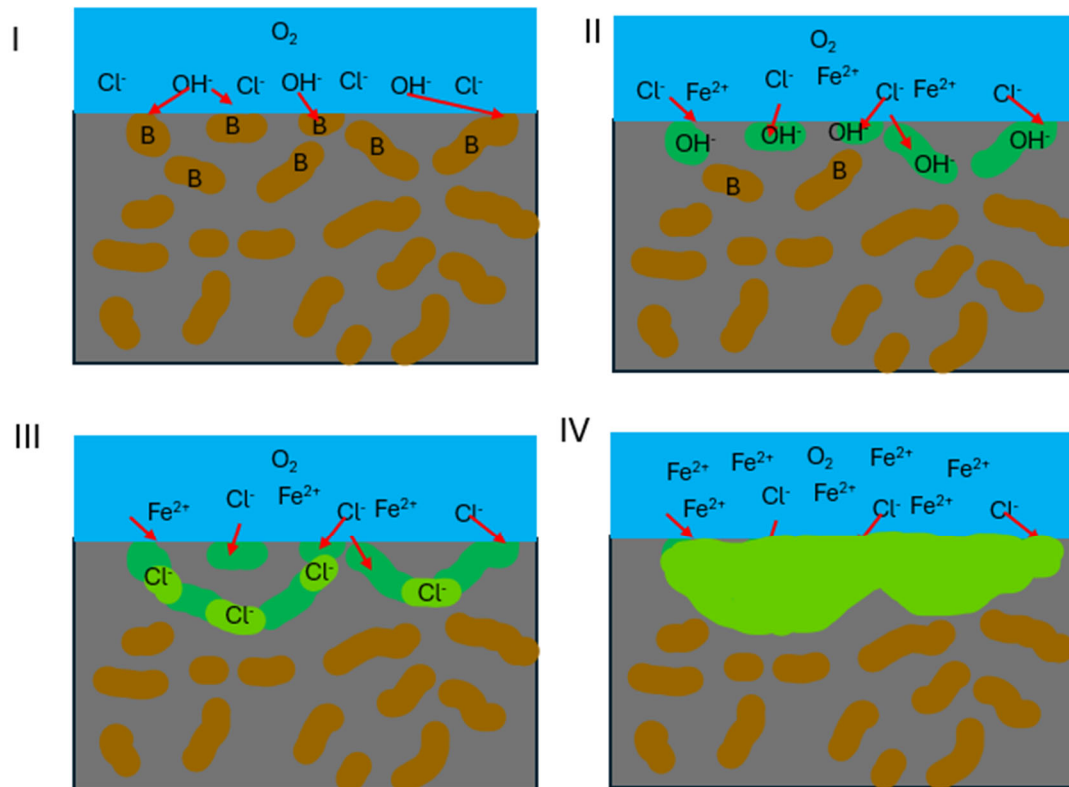


Figure 8. Corrosion mechanism occurring on CP780.

Some research reported how Fe_3C regions act as cathodes, provoking ferrite to act as an anode [98]. For the case of bainite complex-phase steels, parameters such as microstructure and the chemical composition of each phase play an essential role in generating microgalvanic corrosion cells [99]. The dissolution of AHSSs with the presence of ferrite/bainite phases presents the beginning of the corrosion process in the grain boundaries of the ferrite phase when exposed to NaCl [98,99]. For that reason, self-corrosion occurs in the bainite phase.

5. Conclusions

According to the results of the research, it can be concluded that:

- The E-coat increases corrosion resistance of CP780 by more than 1000 times (9.31×10^2 , $7.84 \times 10^2 \Omega \cdot \text{cm}^2$ vs. 94.85×10^4 , $25.82 \times 10^5 \Omega \cdot \text{cm}^2$).
- Phosphate pretreatment increases corrosion resistance from 784 to 1979 $\Omega \cdot \text{cm}^2$; however, it does not reduce the galvanic cell that produces CP780 corrosion.
- The corrosion mechanism of CP780 is the galvanic couple, due to the different phases that have, principally, the bainite, which acts as an anode, so that the corrosion process begins as a localized attack (pitting), and converts after some time to a uniform corrosion process across the surface.

- The E-coat significantly increases the corrosion resistance of CP780; however, the coating is irregular, so the results obtained by Wavelets, HHT, and RP showed a predominance of localized attacks on the surface.
- Analyzing EN signal methods such as Wavelets, HHT, and RP is recommended to determine the corrosion type and mechanism. Also, Z_n0 is a good indicator of the corrosion resistance of materials.

Author Contributions: Conceptualization, F.A.-C. and C.G.-T., methodology, M.L.-B., J.O.-C., J.C.M., G.S.-H., J.M.J.-M., M.A.B.-Z. and F.E.-L.; data curation, F.A.-C., C.G.-T., M.L.-B., G.S.-H., D.N.-M., F.A.-C., M.A.B.-Z. and F.E.-L.; formal analysis, F.A.-C., C.G.-T., J.M.J.-M., J.C.M., M.A.B.-Z., J.O.-C., D.N.-M., M.L.-B. and C.G.-T.; writing—review and editing, F.A.-C., J.M.J.-M. and C.G.-T. All authors have read and agreed to the published version of the manuscript.

Funding: This research received no external funding.

Data Availability Statement: The original contributions presented in this study are included in the article. Further inquiries can be directed to the corresponding authors.

Acknowledgments: The authors would like to thank the UANL-CA-316 working group and Universidad Autónoma de Nuevo León (UANL) for the facilities provided for this investigation.

Conflicts of Interest: The authors declare no conflicts of interest.

References

1. Gould, J.E.; Khurana, S.P.; Li, T. Predictions of Microstructures When Welding Automotive Advanced High-Strength Steels. *Weld. J.* **2006**, *85*, 111.
2. Liang, X.; Wang, Y.; Chen, Y.; Deng, S. Advances in Emission Regulations and Emission Control Technologies for Internal Combustion Engines. *SAE Int. J. Sustain. Transp. Energy Environ. Policy* **2021**, *2*, 101–119. [[CrossRef](#)]
3. Lopez-Cortez, V.H.; Reyes-Valdes, F.A. Undefined Understanding Resistance Spot Welding of Advanced High-Strength Steels. *Weld. J.* **2008**, *87*, 36–40.
4. Escalona Gómez, A.; Delgado Espino, M.; Lara-Banda, M.d.R.; Almeraya Calderón, F. Electrochemical Characterization of Advanced High Strength Steel DP 780 MPa. *Miner. Met. Mater. Ser.* **2020**, *149*, 571–580. [[CrossRef](#)]
5. Castillo Gutiérrez, D.E.; Angarita Moncaleano, I.I.; Rodríguez Baracaldo, R.; Castillo Gutiérrez, D.E.; Angarita Moncaleano, I.I.; Rodríguez Baracaldo, R. Caracterización Microestructural y Mecánica de Aceros de Fase Dual (Ferrita-Martensita), Obtenidos Mediante Procesos Térmicos y Termomecánicos. *Ingeniare. Rev. Chil. Ing.* **2018**, *26*, 430–439. [[CrossRef](#)]
6. Romero-Orozco, A.J.; Taha-Tijerina, J.J.; Luna-Alanís, R.; De López-Morelos, V.H.; Ramírez-López, M.D.C.; Salazar-Martínez, M.; Curiel-López, F.F. Evaluation of Microstructural and Mechanical Behavior of AHSS CP780 Steel Welded by GMAW-Pulsed and GMAW-Pulsed-Brazing Processes. *Metals* **2022**, *12*, 530. [[CrossRef](#)]
7. Macdonald, J.R. Frequency Response of Unified Dielectric and Conductive Systems Involving an Exponential Distribution of Activation Energies. *J. Appl. Phys.* **1985**, *58*, 1955–1970. [[CrossRef](#)]
8. Montoya-Rangel, M.; Garza-Montes-de-Oca, N.F.; Gaona-Tiburcio, C.; Almeraya-Calderón, F. Corrosion mechanism of advanced high strength dual-phase steels by electrochemical noise analysis in chloride solutions. *Mater. Today Commun.* **2023**, *35*, 105663. [[CrossRef](#)]
9. Montoya-Rangel, M.; de Garza-Montes, O.N.; Gaona-Tiburcio, C.; Colás, R.; Cabral-Miramontes, J.; Nieves-Mendoza, D.; Maldonado-Bandala, E.; Chacón-Nava, J.; Almeraya-Calderón, F. Electrochemical noise measurements of advanced high-strength steels in different solutions. *Metals* **2020**, *10*, 1232. [[CrossRef](#)]
10. Almeraya-Calderón, F.; Montoya-Rangel, M.; Nieves-Mendoza, D.; Jáquez-Muñoz, J.M.; Baltazar-Zamora, M.A.; Landa-Ruiz, L.; Lara-Banda, M.; Maldonado-Bandala, E.; Estupiñan-Lopez, F.; Gaona-Tiburcio, C. Frequency–Time Domain Analysis Based on Electrochemical Noise of Dual-Phase (DP) and Ferrite–Bainite (FB) Steels in Chloride Solutions for Automotive Applications. *Metals* **2024**, *14*, 1208. [[CrossRef](#)]
11. Koch, G. Cost of Corrosion. In *Trends in Oil and Gas Corrosion Research and Technologies: Production and Transmission*; Woodhead Publishing: Cambridge, UK, 2017; pp. 3–30, ISBN 9780081012192.
12. Virmani, P. *Corrosion Cost and Preventive Strategies in the United States*, Publication No. FHWA-RD-01-156; Federal Highway Administration: Washington, DC, USA, 2002.
13. Bachert, J.; Rahman, A.H.M.E.; Abu-Ayyad, M. Anti-Corrosive Coating Using Recycled High Density Polyethylene for Automotive Chassis. *ASME Int. Mech. Eng. Congr. Expo. Proc.* **2019**, *12*, V012T11A015. [[CrossRef](#)]

14. Asundi, A.; Choi, A.Y.N. Fiber Metal Laminates: An Advanced Material for Future Aircraft. *J. Mater. Process. Technol.* **1997**, *63*, 384–394. [CrossRef]
15. Shi, X.; Fay, L.; Yang, Z.; Nguyen, T.A.; Liu, Y. Corrosion of Deicers to Metals in Transportation Infrastructure: Introduction and Recent Developments. *Corros. Rev.* **2009**, *27*, 23–52. [CrossRef]
16. Duarte, T.; Meyer, Y.A.; Osório, W.R. The Holes of Zn Phosphate and Hot Dip Galvanizing on Electrochemical Behaviors of Multi-Coatings on Steel Substrates. *Metals* **2022**, *12*, 863. [CrossRef]
17. Ghanbari, A.; Attar, M.M. Surface Free Energy Characterization and Adhesion Performance of Mild Steel Treated Based on Zirconium Conversion Coating: A Comparative Study. *Surf. Coat. Technol.* **2014**, *246*, 26–33. [CrossRef]
18. Tegehall, P.E.; Vannerberg, N.G. Nucleation and Formation of Zinc Phosphate Conversion Coating on Cold-Rolled Steel. *Corros. Sci.* **1991**, *32*, 635–652. [CrossRef]
19. Vakili, H.; Ramezanzadeh, B.; Amini, R. The Corrosion Performance and Adhesion Properties of the Epoxy Coating Applied on the Steel Substrates Treated by Cerium-Based Conversion Coatings. *Corros. Sci.* **2015**, *94*, 466–475. [CrossRef]
20. Tian, Y.; Huang, H.; Wang, H.; Xie, Y.; Sheng, X.; Zhong, L.; Zhang, X. Accelerated Formation of Zinc Phosphate Coatings with Enhanced Corrosion Resistance on Carbon Steel by Introducing α -Zirconium Phosphate. *J. Alloys Compd.* **2020**, *831*, 154906. [CrossRef]
21. Arthanareeswari, M.; Kamaraj, P.; Tamilselvi, M.; Devikala, S. A Low Temperature Nano TiO₂ Incorporated Nano Zinc Phosphate Coating on Mild Steel with Enhanced Corrosion Resistance. *Mater. Today Proc.* **2018**, *5*, 9012–9025. [CrossRef]
22. Reichinger, M.; Bremser, W.; Dornbusch, M. Interface and Volume Transport on Technical Cathodic Painting: A Comparison of Steel, Hot-Dip Galvanised Steel and Aluminium Alloy. *Electrochim. Acta* **2017**, *231*, 135–152. [CrossRef]
23. Dehri, I.; Erbil, M. The Effect of Relative Humidity on the Atmospheric Corrosion of Defective Organic Coating Materials: An EIS Study with a New Approach. *Corros. Sci.* **2000**, *42*, 969–978. [CrossRef]
24. Deflorian, F.; Fedrizzi, L.; Rossi, S.; Buratti, F.; Bonora, P.L. Electrochemical Characterisation of Organic Coatings for the Automotive Industry. *Prog. Org. Coat.* **2000**, *39*, 9–13. [CrossRef]
25. Suay, J.J.; Rodríguez, M.T.; Razaq, K.A.; Carpio, J.J.; Saura, J.J. The Evaluation of Anticorrosive Automotive Epoxy Coatings by Means of Electrochemical Impedance Spectroscopy. *Prog. Org. Coat.* **2003**, *46*, 121–129. [CrossRef]
26. Deflorian, F.; Rossi, S. An EIS Study of Ion Diffusion through Organic Coatings. *Electrochim. Acta* **2006**, *51*, 1736–1744. [CrossRef]
27. Tiyyagura, H.R.; Kumari, S.; Mohan, M.K.; Pant, B.; Nageswara Rao, M. Degradation Behavior of Metastable β Ti-15-3 Alloy for Fastener Applications. *J. Alloys Compd.* **2019**, *775*, 518–523. [CrossRef]
28. Shkirskiy, V.; King, A.D.; Gharbi, O.; Volovitch, P.; Scully, J.R.; Ogle, K.; Birbilis, N. Revisiting the Electrochemical Impedance Spectroscopy of Magnesium with Online Inductively Coupled Plasma Atomic Emission Spectroscopy. *ChemPhysChem* **2015**, *16*, 536–539. [CrossRef]
29. Carley-Clopton, A.; Findley, K.O.; De Moor, E.; Comstock, R.J. Evaluation of Aging and Zn-Coating Effects on Sheared Edge Formability in Sheet Steels. *Int. Symp. New Dev. Adv. High-Strength Sheet Steels AHSS* **2023**, *7*, 86–95. [CrossRef]
30. Scharf, R.; Muhr, A.; Stellnberger, K.H.; Faderl, J.; Holzer, C.; Mori, G. Hydrogen Embrittlement of High Strength Steel under in Situ Corrosive Charging Conditions and Tensile Load. *Mater. Corros.* **2017**, *68*, 95–104. [CrossRef]
31. Wint, N.; Leung, J.; Sullivan, J.H.; Penney, D.J.; Gao, Y. The Galvanic Corrosion of Welded Ultra-High Strength Steels Used for Automotive Applications. *Corros. Sci.* **2018**, *136*, 366–373. [CrossRef]
32. Meddings, N.; Heinrich, M.; Overney, F.; Lee, J.S.; Ruiz, V.; Napolitano, E.; Seitz, S.; Hinds, G.; Raccichini, R.; Gaberšček, M.; et al. Application of Electrochemical Impedance Spectroscopy to Commercial Li-Ion Cells: A Review. *J. Power Sources* **2020**, *480*, 228742. [CrossRef]
33. Venezuela, J.; Liu, Q.; Zhang, M.; Zhou, Q.; Atrens, A. A Review of Hydrogen Embrittlement of Martensitic Advanced High-Strength Steels. *Corros. Rev.* **2016**, *34*, 153–186. [CrossRef]
34. Midea, S.J.; Pfaffmann, G.D. Heat Treating: Including Steel Heat Treating in the New Millennium: An International Symposium in Honor of Professor George Krauss, 1–4 November 1999: Proceedings of the 19th Conference. Available online: <https://searchworks.stanford.edu/view/12930083> (accessed on 2 January 2025).
35. Reyes, A.E.S.; Rodriguez, G.L.; Parra, J.R.G.; Lemus, V.H.M. Microstructural Characterization and Corrosion Behavior of Similar and Dissimilar Welded Advanced High-Strength Steels (AHSS) by Rotary Friction Welding. *Materials* **2024**, *17*, 918. [CrossRef] [PubMed]
36. Hill, H.; Raab, U.; Weber, S.; Theisen, W.; Wollmann, M.; Wagner, L. Influence of Heat Treatment on the Performance Characteristics of a Plastic Mold Steel. *Steel Res. Int.* **2011**, *82*, 1290–1296. [CrossRef]
37. Dubent, S.; Mazard, A. Characterization and Corrosion Behaviour of Grade 2 Titanium Used in Electrolyzers for Hydrogen Production. *Int. J. Hydrogen Energy* **2019**, *44*, 15622–15633. [CrossRef]
38. Franceschi, M.; Pezzato, L.; Settini, A.G.; Gennari, C.; Pigato, M.; Polyakova, M.; Konstantinov, D.; Brunelli, K.; Dabalà, M. Effect of Different Austempering Heat Treatments on Corrosion Properties of High Silicon Steel. *Materials* **2021**, *14*, 288. [CrossRef] [PubMed]

39. Prando, D.; Brenna, A.; Diamanti, M.V.; Beretta, S.; Bolzoni, F.; Ormellese, M.; Pedferri, M.P. Corrosion of Titanium: Part 2: Effects of Surface Treatments. *J. Appl. Biomater. Funct. Mater.* **2018**, *16*, 3–13. [[CrossRef](#)] [[PubMed](#)]
40. Jabłońska, M.; Michalik, R. Studies on the Corrosion Properties of High-Mn Austenitic Steels. *Solid State Phenom.* **2015**, *227*, 75–78. [[CrossRef](#)]
41. Bhadeshia, H.; Honeycombe, R. *Steels: Microstructure and Properties*; Elsevier: Amsterdam, The Netherlands, 2017.
42. Kuziak, R.; Kawalla, R.; Waengler, S. Advanced High Strength Steels for Automotive Industry. *Arch. Civ. Mech. Eng.* **2008**, *8*, 103–117. [[CrossRef](#)]
43. Wei, J.; Dong, J.; Zhou, Y.; He, X.; Wang, C.; Ke, W. Influence of the Secondary Phase on Micro Galvanic Corrosion of Low Carbon Bainitic Steel in NaCl Solution. *Mater. Charact.* **2018**, *139*, 401–410. [[CrossRef](#)]
44. Wang, Z.F.; Li, P.H.; Guan, Y.; Chen, Q.F.; Pu, S.K. The Corrosion Resistance of Ultra-Low Carbon Bainitic Steel. *Corros. Sci.* **2009**, *51*, 954–961. [[CrossRef](#)]
45. Liu, W.; Zhou, Q.; Li, L.; Wu, Z.; Cao, F.; Gao, Z. Effect of Alloy Element on Corrosion Behavior of the Huge Crude Oil Storage Tank Steel in Seawater. *J. Alloys Compd.* **2014**, *598*, 198–204. [[CrossRef](#)]
46. Mansfeld, F. Models for the Impedance Behavior of Protective Coatings and Cases of Localized Corrosion. *Electrochim. Acta* **1993**, *38*, 1891–1897. [[CrossRef](#)]
47. Silverman, D.C. Tutorial on Cyclic Potentiodynamic Polarization Technique. In Proceedings of the NACE—International Corrosion Conference Series, San Diego, CA, USA, 22–27 March 1998.
48. Silverman, D.C. Practical Corrosion Prediction Using Electrochemical Techniques. In *Uhlig's Corrosion Handbook*, 3rd ed.; Wiley: Hoboken, NJ, USA, 2011; pp. 1129–1166. [[CrossRef](#)]
49. Sanchez-Amaya, J.M.; Cottis, R.A.; Botana, F.J. Shot Noise and Statistical Parameters for the Estimation of Corrosion Mechanisms. *Corros. Sci.* **2005**, *47*, 3280–3299. [[CrossRef](#)]
50. Bertocci, U.; Kruger, J. Studies of Passive Film Breakdown by Detection and Analysis of Electrochemical Noise. *Surf. Sci.* **1980**, *101*, 608–618. [[CrossRef](#)]
51. Kearns, J.R.; Scully, J.R.; Roberge, P.R.; Reichert, D.L.; Dawson, J.L. *Electrochemical Noise Measurement for Corrosion Applications*; ASTM International: West Conshohocken, PA, USA, 2015; ISBN 080312032X.
52. Eden, D.A. Electrochemical Noise—The First Two Octaves. In Proceedings of the NACE—International Corrosion Conference Series, San Diego, CA, USA, 22–27 March 1998.
53. Eden, D.A.; Rothwell, A.N. *Electrochemical Noise Data: Analysis, Interpretation and Presentation*; Corrosion/92, Paper No. 292; NACE: Houston, TX, USA, 1992; pp. 1–12.
54. Bertocci, U.; Gabrielli, C.; Huet, F.; Keddam, M.; Rousseau, P. Noise Resistance Applied to Corrosion Measurements: II. Experimental Tests. *J. Electrochem. Soc.* **1997**, *144*, 37–43. [[CrossRef](#)]
55. Reid, S.A.; Eden, D.A. Assessment of Corrosion. US9264824B1, 24 July 2001.
56. Mansfeld, F.; Sun, Z.; Hsu, C.H.; Nagiub, A. Concerning Trend Removal in Electrochemical Noise Measurements. *Corros. Sci.* **2001**, *43*, 341–352. [[CrossRef](#)]
57. Cottis, R.; Turgoose, S. *Electrochemical Impedance and Noise*; NACE International: Shanghai, China, 1999; p. 153.
58. Mansfeld, F.; Sun, Z. Technical Note: Localization Index Obtained from Electrochemical Noise Analysis. *Corrosion* **1999**, *55*, 915–918. [[CrossRef](#)]
59. Legat, A.; Dolecček, V. Corrosion Monitoring System Based on Measurement and Analysis of Electrochemical Noise. *Corrosion* **1995**, *51*, 295–300. [[CrossRef](#)]
60. Uruchurtu, J.C.; Dawson, J.L. Noise Analysis of Pure Aluminum under Different Pitting Conditions. *Corrosion* **1987**, *43*, 19–26. [[CrossRef](#)]
61. Bertocci, U.; Huet, F.; Nogueira, R.P.; Rousseau, P. Drift Removal Procedures in the Analysis of Electrochemical Noise. *Corrosion* **2002**, *58*, 337–347. [[CrossRef](#)]
62. Homborg, A.M.; Tinga, T.; Van Westing, E.P.M.; Zhang, X.; Ferrari, G.M.; De Wit, J.H.W.; Mol, J.M.C. A Critical Appraisal of the Interpretation of Electrochemical Noise for Corrosion Studies. *Corrosion* **2014**, *70*, 971–987. [[CrossRef](#)]
63. Bertocci, U.; Huet, F. Noise Analysis Applied to Electrochemical Systems. *Corrosion* **1995**, *51*, 131–144. [[CrossRef](#)]
64. Brockwell, P.J.; Davis, R.A. *Introduction to Time Series and Forecasting*; Springer Nature: Dordrecht, GX, The Netherlands, 2016. [[CrossRef](#)]
65. Homborg, A.M.; Oonincx, P.J.; Mol, J.M.C. Wavelet Transform Modulus Maxima and Holder Exponents Combined with Transient Detection for the Differentiation of Pitting Corrosion Using Electrochemical Noise. *Corrosion* **2018**, *74*, 1001–1010. [[CrossRef](#)]
66. Cai, C.; Zhang, Z.; Cao, F.; Gao, Z.; Zhang, J.; Cao, C. Analysis of Pitting Corrosion Behavior of Pure Al in Sodium Chloride Solution with the Wavelet Technique. *J. Electroanal. Chem.* **2005**, *578*, 143–150. [[CrossRef](#)]
67. Homborg, A.M.; van Westing, E.P.M.; Tinga, T.; Zhang, X.; Oonincx, P.J.; Ferrari, G.M.; de Wit, J.H.W.; Mol, J.M.C. Novel Time–Frequency Characterization of Electrochemical Noise Data in Corrosion Studies Using Hilbert Spectra. *Corros. Sci.* **2013**, *66*, 97–110. [[CrossRef](#)]

68. Garcia-Ochoa, E. Recurrence Plots: A New Methodology for Electrochemical Noise Signal Analysis. *J. Electroanal. Chem.* **2020**, *864*, 114092. [[CrossRef](#)]
69. Marwan, N.; Carmen Romano, M.; Thiel, M.; Kurths, J. Recurrence Plots for the Analysis of Complex Systems. *Phys. Rep.* **2007**, *438*, 237–329. [[CrossRef](#)]
70. Marwan, N.; Kraemer, K.H. Trends in Recurrence Analysis of Dynamical Systems. *Eur. Phys. J. Spec. Top.* **2023**, *232*, 5–27. [[CrossRef](#)]
71. Arellano-Pérez, J.H.; Escobar-Jiménez, R.F.; Granados-Lieberman, D.; Gómez-Aguilar, J.F.; Uruchurtu-Chavarín, J.; Alvarado-Martínez, V.M. Electrochemical Noise Signals Evaluation to Classify the Type of Corrosion Using Synchrosqueezing Transform. *J. Electroanal. Chem.* **2019**, *848*, 113249. [[CrossRef](#)]
72. Ren, Z.; Li, Q.; Yang, X.; Wang, J. A Novel Method for Identifying Corrosion Types and Transitions Based on Adaboost and Electrochemical Noise. *Anti-Corros. Methods Mater.* **2023**, *70*, 78–85. [[CrossRef](#)]
73. Ye, Z.; Guan, L.; Li, Y.; Zhong, J.; Liao, L.; Xia, D.; Huang, J. Understanding the Galvanic Corrosion of Cu-Ni Alloy/2205 DSS Couple Using Electrochemical Noise and Microelectrochemical Studies. *Corros. Sci.* **2023**, *224*, 111512. [[CrossRef](#)]
74. ASTM E3-95; Standard Practice for Preparation of Metallographic Specimens. ASTM International: West Conshohocken, PA, USA, 2007.
75. ASTM G199-09; Standard Guide for Electrochemical Noise Measurement. ASTM International: West Conshohocken, PA, USA, 2014.
76. Jáquez-Muñoz, J.M.; Gaona-Tiburcio, C.; Méndez-Ramírez, C.T.; Baltazar-Zamora, M.Á.; Estupinán-López, F.; Bautista-Margulis, R.G.; Cuevas-Rodríguez, J.; Flores-De los Rios, J.P.; Almeraya-Calderón, F. Corrosion of Titanium Alloys Anodized Using Electrochemical Techniques. *Metals* **2023**, *13*, 476. [[CrossRef](#)]
77. Jáquez-Muñoz, J.M.; Gaona-Tiburcio, C.; Méndez-Ramírez, C.T.; Martínez-Ramos, C.; Baltazar-Zamora, M.A.; Santiago-Hurtado, G.; Estupinan-Lopez, F.; Landa-Ruiz, L.; Nieves-Mendoza, D.; Almeraya-Calderon, F. Electrochemical Noise Analysis: An Approach to the Effectivity of Each Method in Different Materials. *Materials* **2024**, *17*, 4013. [[CrossRef](#)]
78. Almeraya-Calderon, F.; Villegas-Tovar, M.; Maldonado-Bandala, E.; Lara-Banda, M.; Baltazar-Zamora, M.A.; Santiago-Hurtado, G.; Nieves-Mendoza, D.; Lopez-Leon, L.D.; Jaquez-Muñoz, J.M.; Estupinán-López, F.; et al. Use of Electrochemical Noise for the Study of Corrosion by Passivated CUSTOM 450 and AM 350 Stainless Steels. *Metals* **2024**, *14*, 341. [[CrossRef](#)]
79. Enestam, S.; Bankiewicz, D.; Tuiremo, J.; Mäkelä, K.; Hupa, M. Are NaCl and KCl Equally Corrosive on Superheater Materials of Steam Boilers? *Fuel* **2013**, *104*, 294–306. [[CrossRef](#)]
80. Marcus, P. (Ed.) *Corrosion Mechanisms in Theory and Practice*, 2nd ed.; CRC Press: Boca Raton, FL, USA, 2002.
81. Shi, Y.Y.; Zhang, Z.; Cao, F.H.; Zhang, J.Q. Dimensional Analysis Applied to Pitting Corrosion Measurements. *Electrochim. Acta* **2008**, *53*, 2688–2698. [[CrossRef](#)]
82. Shibaeva, T.V.; Laurinavichyute, V.K.; Tsirlina, G.A.; Arsenkin, A.M.; Grigorovich, K.V. The Effect of Microstructure and Non-Metallic Inclusions on Corrosion Behavior of Low Carbon Steel in Chloride Containing Solutions. *Corros. Sci.* **2014**, *80*, 299–308. [[CrossRef](#)]
83. Cottis, R.A.; Homborg, A.M.; Mol, J.M.C. The Relationship between Spectral and Wavelet Techniques for Noise Analysis. *Electrochim. Acta* **2016**, *202*, 277–287. [[CrossRef](#)]
84. Suresh, G.; Mudali, U.K. Electrochemical Noise Analysis of Pitting Corrosion of Type 304L Stainless Steel. *Corrosion* **2014**, *70*, 283–293. [[CrossRef](#)]
85. Cappelín, F.; Bjerrum, N.J.; Petrushina, I.M. Electrochemical Noise Measurements of Steel Corrosion in the Molten NaCl-K₂SO₄ System. *J. Electrochem. Soc.* **2005**, *152*, B228. [[CrossRef](#)]
86. Jáquez-Muñoz, J.M.; Gaona-Tiburcio, C.; Cabral-Miramontes, J.; Nieves-Mendoza, D.; Maldonado-Bandala, E.; Olguín-Coca, J.; Estupinán-López, F.; López-León, L.D.; Chacón-Nava, J.; Almeraya-Calderón, F. Frequency Analysis of Transients in Electrochemical Noise of Superalloys Waspaloy and Udimet. *Metals* **2021**, *11*, 702. [[CrossRef](#)]
87. Ortiz-Corona, J.; Uruchurtu-Chavarín, J.; García-Ochoa, E.M.; González-Sánchez, J.A.; Larios-Duran, E.R.; Rodríguez-Gómez, F.J. Monitoring of Silver Alloy Tarnishing in Sulphides by Electrochemical Noise Measurements: Application of Statistical and Recurrence Plot Analysis. *Electrochim. Acta* **2024**, *495*, 144388. [[CrossRef](#)]
88. Luo, B.; Wei, Q.; Hu, S.; Manoach, E.; Deng, T.; Cao, M. A Novel Cross-Domain Identification Method for Bridge Damage Based on Recurrence Plot and Convolutional Neural Networks. *J. Vibroeng.* **2024**, *26*, 1040–1061. [[CrossRef](#)]
89. Calabrese, L.; Galeano, M.; Proverbio, E. Identifying Corrosion Forms on Synthetic Electrochemical Noise Signals by the Hilbert–Huang Transform Method. *Corros. Eng. Sci. Technol.* **2018**, *53*, 492–501. [[CrossRef](#)]
90. Lin, R.L.; Li, W.Y.; Li, L.; Liao, C.J. High-Dissolution Mechanism of Ti–48Al–2Cr–2Nb Alloy in Electrochemical Machining from a Nonlinear Dynamic Perspective. *Adv. Eng. Mater.* **2024**, *26*, 2302083. [[CrossRef](#)]
91. Martínez-Villafañe, A.; Almeraya-Calderón, F.; Gaona-Tiburcio, C.; Gonzalez-Rodriguez, J.; Porcayo-Calderón, J. High-Temperature Degradation and Protection of Ferritic and Austenitic Steels in Steam Generators. *J. Mater. Eng. Perform.* **1998**, *7*, 108–113. [[CrossRef](#)]

92. Martínez-Ramos, C.; Olguin-Coca, J.; Lopez-Leon, L.D.; Gaona-Tiburcio, C.; Lara-Banda, M.; Maldonado-Bandala, E.; Castañeda-Robles, I.; Jaquez-Muñoz, J.M.; Cabral-Miramontes, J.; Nieves-Mendoza, D.; et al. Electrochemical Noise Analysis Using Experimental Chaos Theory, Power Spectral Density and Hilbert–Huang Transform in Anodized Aluminum Alloys in Tartaric–Phosphoric–Sulfuric Acid Solutions. *Metals* **2023**, *13*, 1850. [[CrossRef](#)]
93. Kalhor, A.; Soleimani, M.; Mirzadeh, H.; Uthaisangsk, V. A Review of Recent Progress in Mechanical and Corrosion Properties of Dual Phase Steels. *Arch. Civ. Mech. Eng.* **2020**, *20*, 85. [[CrossRef](#)]
94. Seifert, M.; Wieskämper, D.; Tonfeld, T.; Huth, S. Corrosion Properties of a Complex Multi-Phase Martensitic Stainless Steel Depending on the Tempering Temperature. *Mater. Corros.* **2015**, *66*, 1290–1298. [[CrossRef](#)]
95. Jáquez-Muñoz, J.M.; Gaona-Tiburcio, C.; Mendez-Ramirez, C.T.; Carrera-Ramirez, M.G.; Baltazar-Zamora, M.A.; Santiago-Hurtado, G.; Lara-Banda, M.; Estupiñan-Lopez, F.; Nieves-Mendoza, D.; Almeraya-Calderon, F. Corrosion of Anodized Titanium Alloys. *Coatings* **2024**, *14*, 809. [[CrossRef](#)]
96. Qu, S.; Pang, X.; Wang, Y.; Gao, K. Corrosion Behavior of Each Phase in Low Carbon Microalloyed Ferrite–Bainite Dual-Phase Steel: Experiments and Modeling. *Corros. Sci.* **2013**, *75*, 67–77. [[CrossRef](#)]
97. Martínez-Aparicio, B.; Gaona-Tiburcio, C.; Almeraya-Calderon, F.; Goldsberry, R.; Castaneda, H. Evaluation of Passive Films on 17-7PH and 410 Stainless Steel Exposed to NaCl Solution. *Materials* **2024**, *17*, 4060. [[CrossRef](#)] [[PubMed](#)]
98. Liu, C.; Cheng, X.; Dai, Z.; Liu, R.; Li, Z.; Cui, L.; Chen, M.; Ke, L. Synergistic Effect of Al₂O₃ Inclusion and Pearlite on the Localized Corrosion Evolution Process of Carbon Steel in Marine Environment. *Materials* **2018**, *11*, 2277. [[CrossRef](#)] [[PubMed](#)]
99. Moon, A.P.; Sangal, S.; Layek, S.; Giribaskar, S.; Mondal, K. Corrosion Behavior of High-Strength Bainitic Rail Steels. *Metall. Mater. Trans. A Phys. Metall. Mater. Sci.* **2015**, *46*, 1500–1518. [[CrossRef](#)]

Disclaimer/Publisher’s Note: The statements, opinions and data contained in all publications are solely those of the individual author(s) and contributor(s) and not of MDPI and/or the editor(s). MDPI and/or the editor(s) disclaim responsibility for any injury to people or property resulting from any ideas, methods, instructions or products referred to in the content.